Waveguide-enhanced grazing-incidence small-angle x-ray scattering of buried nanostructures in thin films

Zhang Jiang, Dong Ryeol Lee, Suresh Narayanan, Jin Wang, and Sunil K. Sinha

Phys. Rev. B **84**, 075440 — Published 9 August 2011

DOI: 10.1103/PhysRevB.84.075440

Waveguide-enhanced grazing-incidence small-angle x-ray scattering of buried nanostructures in thin films

Zhang Jiang,* Dong Ryeol Lee,† Suresh Narayanan, and Jin Wang‡
X-ray Science Division, Argonne National Laboratory, Argonne, Illinois 60439

Sunil K. Sinha
Department of Physics, University of California San Diego, La Jolla, California 92093
(Dated: May 16, 2011)

X-ray standing waves (XSW) generated by the interference of the scattered x-rays from parallel surfaces of a thin film, the so-called waveguide effect, can be used to enhance the scatterings from certain depths of the film. Used in combination with grazing-incidence small-angle x-ray scattering (GISAXS), this resonance effect provides depth sensitivity to extract buried structures in thin films of polymer and polymer/nanoparticle nanocomposite, which are not readily accessible by most surface techniques, such as scanning probe microscopy. We developed a rigorous theory of the diffuse scattering in the framework of the distorted-wave Born approximation (DWBA) using a discretization method analogous to Parratt's recursive formalism. In such a case, the distortion of the electric field of the unperturbed state from the nanostructures of interest is considered in a self-consistent manner. This theory allows a quantitative determination of the buried nanostructures when the x-ray waveguide enhancement is present or the size of the nanostructures of interest is comparable to or larger than the spatial frequency of electric field intensity distribution. A unique capability afforded by this theory is that a nanometer or even subnanometer spatial resolution can be achieved in the depth information of the buried nanostructures.

PACS numbers: 61.05.cf, 62.23.St, 68.55.-a, 81.07.-b

I. INTRODUCTION

Waveguide-based enhancement of the electric field is usually created between parallel surfaces separated by a medium with a different electron density.[1–3] However, the generated x-ray standing wave (XSW), whose periodicity is determined by the incident angle, is not confined within the waveguide.[4] It can extend to the boundary media and even beyond the top surface. The resonance (in the context of waveguide effect instead of the spectroscopic sense) modes in a thin-film-based x-ray waveguide are sensitive to the electron density profile (EDP) of the film. At incident angles, which create resonance modes (resonant angles), the electric field intensity (EFI) of the XSW reaches its maximum at a certain depth of the film, yielding an enhancement of the scattering from the structures at that depth level by 1-2 orders of magnitude. Therefore, by scanning the incident angle and using the resonance effect, it is feasible to determine the depth-dependent structures from the incident-angle-dependent grazing-incidence small-angle x-ray scattering (GISAXS) patterns.[5–7]

As a surface probe, GISAXS has several advantages over many conventional characterization techniques. These include scattering enhancement at grazing angles, statistical description of the sample over macroscopic length scales, and ready adaptation to various experimental environments, such as vacuum and controlled gas ambient for *in situ* studies. A comprehensive review of the GISAXS technique for studying surface structures was recently done by Renaud et al.[8] Given the high beam brilliance and intensity from synchrotron x-ray sources, it is feasible to investigate the kinetics and dynamics in thin films and at surfaces when GISAXS is integrated with time-resolved techniques. With these advantages, GISAXS has been applied to a variety of systems, such as nanostructured polymer thin films,[9–18] nanoparticle-polymer composites,[5,6,19–21] and supported nanoislands.[22–28] Due to the complex data processing involving the distorted-wave Born approximation (DWBA), GISAXS analyses in early days were often performed in a qualitative manner, where only scattering peak positions and widths are identified. The quantitative analysis theories and experimental applications have been extensively reviewed,[8] where various DWBA approximations were discussed and compared for a variety of systems. However, most models were developed either for single-layer films[10,29] or for supported nanoislands.[30,31] While these analysis models can be applied in most cases, they may not be precise when the nanostructures of interest significantly perturb the scattering potentials or when the size of the nanostructures is comparable to the EFI period. A graded DWBA has been recently developed to account for the perturbation induced by high surface concentration of nanoislands supported on substrates.[32] However, in the presence of the XSW-induced waveguide effect, the intrinsic interference arising from the depth-dependent EFI and the scattering from the buried nanostructures becomes significant, especially at grazing angles between the critical angles of total external reflection for the film and the substrate. Such effects can invalidate some of the basic assumptions used in conventional DWBA theories.[8] For example, the EFI distribution can vary drastically at resonant incident angles. By scanning the incidence angle across these resonant angles at wave guiding conditions, various depths of the buried structures are illuminated, hence giving clues regarding the structures at those depths. Due to these effects, most of the current existing DWBA theories can only explain the scattering data taken either well below the film critical angle or above the substrate critical angle, while being not effective in yielding quantitative agreement for data taken at angles between these critical angles, especially near the resonant angles. Most importantly, it is exactly the scattering data in this range that reveals the depth-dependent information of the sample. There have been recent GISAXS and diffuse scattering studies using a quantitative analysis taking into account the depth dependence of the EFI. These studies took advantage of the resonant XSW intensities either to enhance the scattering from buried nanoparticle layers in thin films[5,6,20] or to quantitatively separate bulk from interface scattering.[33–35] In addition, a significant development has been made to characterize the vertical correlations between the nanoparticles and multilayer interfaces,[7] where the vertical roughness correlations have been successfully measured in the presence of the waveguide effect so as to reveal the degree of the topographical replication of the monolayer nanoparticles across multi-interfaces.

In this work, we present a more comprehensive and general treatment of the DWBA method for GISAXS analysis, which can be applied to particles of arbitrary size, shape and distribution buried in film. This method self-consistently allows for the average perturbing effect of the buried particles on the EFI depth distribution and can thus, in principle, give the most accurate description of the scattering within the DWBA. It involves the slicing of the sample into a sufficiently large number of effective layers, similar to the well-known Parratt method for calculating the reflectivity from films of arbitrary density profiles.[36] This can be considered as a generalization of the Parratt method to off-specular scattering. In the presence of XSW, a single nanoparticle is not exposed to a uniform electric field and cannot be treated by a conventional kinematic form factor as widely used in Born approximation as well as in many conventional DWBA theories. Instead, the interference of the EFI and the shape of the particle must be measured in terms of the depth integration over the discretized particle form factor multiplied by its subjected depth-dependent EFI, with the integration step size determined by the spatial variation the EFI distribution, as in the Parratt algorithm for x-ray reflectivities from films[36] or the iso-strain model for grazing-incidence diffraction from the strain field of quantum dots.[37] Take a vertical cylinder spanned from the substrate to the film surface for example.

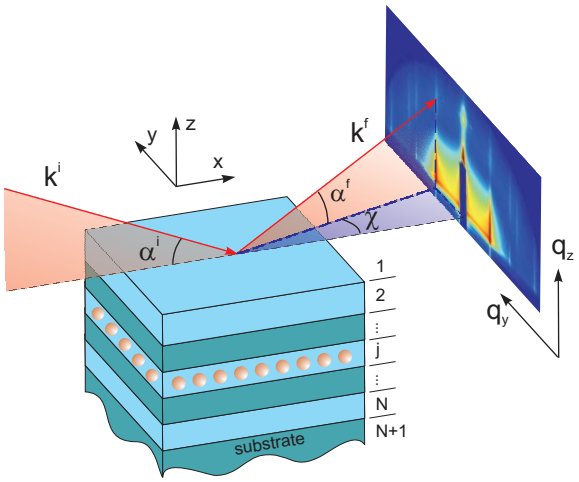

FIG. 1. GISAXS geometry from a multilayer film of embedded nanostructures. The incident and exit wave vectors are $\boldsymbol{k}^i$ and $\boldsymbol{k}^f$. The incident and exit angles are α^i and α^f. The angle out of the scattering plane is χ.

In the Born approximation and conventional DWBA theories, this cylinder sees a uniform electric field so that the form factor is simply a Fourier transform of the shape function. However, in the presence of the XSW, which gives rise to a modulation to the EFI by 1-2 orders of magnitude at resonant angles between the critical angles of the film and the substrate, this cylinder sees an intensity distribution of the electric field. At the 1st resonant angle, only a small portion of the cylinder is illuminated, while at the 2nd resonant angle, effectively two cylinders stacked on each other and spaced with a certain distance by the period of the standing wave are illuminated. Therefore, the scattering intensity should be a coherent sum of the integration of discretized form factor multiplied by corresponding electric field. These effects have already been partially taken into account experimentally for self-directed assembly in nanoparticle-diblock copolymer mixtures.[19]

To treat the XSW effect systematically, the present study is organized as follows. In section II A, the diffuse differential cross section using the DWBA theory for a multilayer film with embedded nanostructures is developed for general purposes. Our discretized multilayer DWBA theory can be readily reduced to the conventional scattering theories under certain special circumstances. The XSW effect and the EFI enhancement are intrinsically included in this theory and are illustrated with several examples in sections II B and II C by comparing to conventional scattering theories. The experimental resolution of the XSW effect is discussed in section II D. Case studies taking into the waveguide effect using the multilayer DWBA theory are discussed in section III A. In addition to the nanocomposite films with nanoparticles or nanostructures of small dimensions,[5,7] this theory can also be applied in general to either embedded or supported objects whose size effect cannot be simply treated using kinematic form factor due to significant EFI variations across the object of interest, examples for which are given in sections III B and III C.

II. THEORETICAL BACKGROUND

A. Multilayer distorted-wave Born approximation for films with buried structures

The structure of an object can be determined through a scattering measurement, which is often quantified by a differential cross section — the probability to observe a scattered photon per unit solid angle per unit incident flux at a given scattering direction. In this section, we use DWBA theory[38,39] to derive the differential cross section for a film with depth-dependent buried nanostructures (e.g., nanoparticles embedded in a polymer matrix). The scattering geometry is shown in Fig. 1. The buried structure of interest does not have to be small so as to be confined within one layer physically. Instead, it can extend to multilayers. When its size is comparable or larger than the EFI variation, a discretization of the structure in the DWBA formalism is mandatory, as discussed below.

Similar to Parratt's approach, we assume that the film consists of $N-1$ layers. Including the topmost air or vacuum and bottommost substrate semi-infinite layers, there are $N+1$ layers in total, each extending to infinity in the xy plane. The number of layers is chosen so that neither the distribution and the average in-plane electron density, nor the electric field intensity (EFI), varies significantly as a function of depth in each layer.

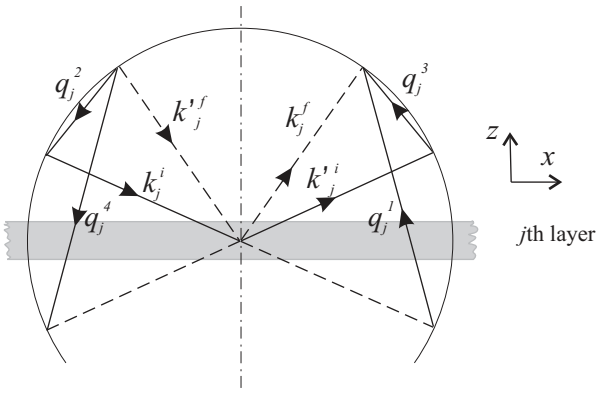

FIG. 2. Schematic of the wave vector transfers q_j^m in the jth layer. They are defined as the vector differences between the wave vectors k^i (incident) and k'^i, and those for the time-reversed state k^f (exit) and k'^f.

We start with the Helmholtz equation

$$(\nabla^2 + k_0^2)|\psi\rangle = 4\pi r_e \rho(\boldsymbol{r})|\psi\rangle, \tag{1}$$

where $|\psi\rangle$ is the wave function, k_0 is the wave vector in the topmost layer ($j = 1$), and r_e is the Thompson scattering constant. The complex electron density $\rho(\boldsymbol{r})$ is related to the index of refraction $n(\boldsymbol{r})$ via $\rho(\boldsymbol{r}) = (k_0^2/4\pi r_e)[1-n^2(\boldsymbol{r})]$. Considering nanostructures or nanoparticles of electron density ρ^{NS} embedded in a matrix of electron density ρ^{MT}, the total electron density $\rho(\boldsymbol{r})$ in the jth layer is written as

$$\rho_j(\boldsymbol{r}_\parallel) = \rho_j^{\mathrm{MT}} + \Delta\rho_j \int_j d\boldsymbol{r}' \delta_j(\boldsymbol{r}_\parallel - \boldsymbol{r}'_\parallel), \tag{2}$$

where the subscript $\parallel$ denotes the in-plane component, $\Delta\rho_j = \rho_j^{\mathrm{NS}} - \rho_j^{\mathrm{MT}}$ is the density difference between the nanostructure and the matrix, and $\delta_j = 1$ and 0 within the nanostructure and the matrix respectively. We rewrite the electron density as

$$\rho_j(\boldsymbol{r}_\parallel) = \overline{\rho}_j + \delta\rho_j(\boldsymbol{r}_\parallel), \tag{3}$$

where the first term, $\overline{\rho}_j = \left\langle \rho_j(\boldsymbol{r}_\parallel) \right\rangle_\parallel$, is the unperturbed scattering potential, and the second term represents the perturbation

$$\delta\rho_j(\boldsymbol{r}_\parallel) = \Delta\rho_j \left[\int_j d\boldsymbol{r}' \delta_j(\boldsymbol{r}_\parallel - \boldsymbol{r}'_\parallel) - \left\langle \int_j d\boldsymbol{r}' \delta_j(\boldsymbol{r}_\parallel - \boldsymbol{r}'_\parallel) \right\rangle_\parallel \right]. \tag{4}$$

Assume a normalized incoming plane wave $\phi^i = e^{\boldsymbol{k}_0 \cdot \boldsymbol{r}}$ incident onto the 1st interface from the topmost layer. For the incident beam, the eigenstate of the unperturbed system ($\delta\rho = 0$) is given by

$$|\psi^i(\boldsymbol{r})\rangle = T^i(z) e^{i\boldsymbol{k}^i(z)\cdot\boldsymbol{r}} + R^i(z) e^{i\boldsymbol{k}'^i(z)\cdot\boldsymbol{r}}, \tag{5}$$

where $\boldsymbol{k}^i(z)$ and $\boldsymbol{k}'^i(z)$ denote the mirrored wave vectors with respect to the surface normal with $k_\parallel^i(z) = k_\parallel'^i(z)$ and $k_z^i(z) = -k_z'^i(z)$. The depth-dependent complex amplitudes of the transmitted and reflected waves for the incident beam are $T^i(z)$ and $R^i(z)$, which can be obtained by Parratt's recursion method.[36,40,41] Using Eq. (5), the EFI at depth z can be calculated via $|T^i(z)e^{ik_z^i(z)z} + R^i(z)e^{ik_z'^i(z)z}|^2$.

Similarly, for the exit beam, we define another eigenstate of the unperturbed system, which is a time-reversed state with incoming wave vector $-\boldsymbol{k}^f(z)$,

$$|\widetilde{\psi}^f(\boldsymbol{r})\rangle = \left[T^f(z)\right]^* e^{i\left[\boldsymbol{k}^f(z)\right]^*\cdot\boldsymbol{r}} + \left[R^f(z)\right]^* e^{i\left[\boldsymbol{k}'^f(z)\right]^*\cdot\boldsymbol{r}}, \tag{6}$$

where $k_\parallel^f(z) = k_\parallel'^f(z)$, $k_z^f(z) = -k_z'^f(z)$ and the asterisks represent the complex conjugates. Similarly, $T^f(z)$ and $R^f(z)$ are the complex amplitudes of the transmitted and reflected waves for the exit beam. In a scattering event,

$\boldsymbol{k}^i(z)$ and $\boldsymbol{k}^f(z)$ represent the wave vectors for the incident beam and the exit beam, respectively (Fig. 1). The relations between $\boldsymbol{k}^i$, $\boldsymbol{k}'^i$, $\boldsymbol{k}^f$ and $\boldsymbol{k}'^f$ are depicted in Fig. 2. The eigenstates for the incident and exit beams are then given by Eq. (5) and Eq. (6), respectively.

The transition matrix $\mathbb{T}$ for scattering between the initial state $|i\rangle$ and the final state $|f\rangle$[42] is

$$\langle f\,|\mathbb{T}|\,i\rangle = 4\pi r_e\left(\left\langle\widetilde{\psi}^f\,|\overline{\rho}|\,\phi^i\right\rangle + \left\langle\widetilde{\psi}^f\,|\delta\rho|\,\psi^i\right\rangle\right). \tag{7}$$

For simplicity, we use $\overline{\rho}^{i\to f}$ and $\delta\rho^{i\to f}$ to denote the two righthand terms in Eq. (7), respectively. The differential cross section is then given by

$$\frac{d\sigma}{d\Omega} = \frac{1}{16\pi^2}\left\langle|\langle f\,|\mathbb{T}|\,i\rangle|^2\right\rangle = r_e^2\left\langle\left|\overline{\rho}^{i\to f} + \delta\rho^{i\to f}\right|^2\right\rangle. \tag{8}$$

For a certain electron density probability distribution, numerous configurational realizations exist, the collection of which is called the ensemble. Given any one of these realizations, the scattering intensity arises from the incoherent spatial average over many coherently illuminated regions (coherent volume). Very frequently, this average does not depend upon the absolute coordinates. Instead, it is only a function of the relative distances between two arbitrarily chosen positions. In this case, the spatial average is equivalent to the ensemble average, which is denoted by <> in Eq. (8). The differential cross section can then be separated into the sum of specular (coherent) and diffuse (incoherent) parts

$$\left(\frac{d\sigma}{d\Omega}\right)_{\text{spec}} = r_e^2\left|\overline{\rho}^{i\to f} + \left\langle\delta\rho^{i\to f}\right\rangle\right|^2, \tag{9}$$

$$\left(\frac{d\sigma}{d\Omega}\right)_{\text{diff}} = r_e^2\left(\left\langle\left|\delta\rho^{i\to f}\right|^2\right\rangle - \left|\left\langle\delta\rho^{i\to f}\right\rangle\right|^2\right). \tag{10}$$

Here, we have used an identity that if B is a fluctuating quantity, $\langle|A+B|^2\rangle = |A+\langle B\rangle|^2 + \langle|B|^2\rangle - |\langle B\rangle|^2$. We will focus on the diffuse scattering. With $\langle\delta\rho\rangle = 0$ in Eq. (4), the second term in the diffuse part vanishes. We also notice that the diffuse scattering arising from the second term of Eq. (4), which is an in-plane averaged electron density and does not depend on $\boldsymbol{r}_\parallel$, exists only at $\boldsymbol{q}_\parallel = 0$. Therefore, this term can be dropped so long as the diffuse scattering away from the specular condition is considered.

Since the electron density distribution of each nanostructure or nanoparticle can be determined by its shape and its location $\boldsymbol{r}^p$, the first term in Eq. (4) can be written as the shape function $P^p(\boldsymbol{r})$ convoluted with particle locations $\sum_p \delta(\boldsymbol{r}-\boldsymbol{r}^p)$, so that

$$\int_j d\boldsymbol{r}'\delta_j(\boldsymbol{r}_\parallel - \boldsymbol{r}'_\parallel) = \sum_p P_j^p(\boldsymbol{r})\otimes\delta_j(\boldsymbol{r}-\boldsymbol{r}^p). \tag{11}$$

According to the the convolution theorem, the Fourier transform of Eq. (11) is the product of the Fourier transforms of the particle shape function and the location, which are nothing else but the form factor $F_j(\boldsymbol{q})$ and the structure factor $S_j(\boldsymbol{q}) = \sum_p e^{i\boldsymbol{q}\cdot\boldsymbol{r}_j^p}$, respectively. Therefore, the diffuse cross section can be approximated by

$$\left(\frac{d\sigma}{d\Omega}\right)_{\text{diff}} \approx r_e^2\left\langle\left|\sum_{m=1}^{4}\sum_{j=1}^{N+1}\Delta\rho_j D_j^m F_j(q_{z,j}^m,\boldsymbol{q}_\parallel)S_j(q_{z,j}^m,\boldsymbol{q}_\parallel)\right|^2\right\rangle, \tag{12}$$

where D_j^m is defined as

$$\begin{aligned} D_j^1 &= T_j^f T_j^i, \quad D_j^2 = R_j^f T_j^i, \\ D_j^3 &= T_j^f R_j^i, \quad D_j^4 = R_j^f R_j^i, \end{aligned} \tag{13}$$

and $\boldsymbol{q}_j^m$ has been split into components $q_{z,j}^m$ and $\boldsymbol{q}_\parallel$

$$\begin{aligned} \boldsymbol{q}_j^1 &= \boldsymbol{k}_j^f - \boldsymbol{k}_j^i = (\boldsymbol{q}_\parallel, q_{z,j}^1) = \left(\boldsymbol{q}_\parallel, k_{z,j}^f - k_{z,j}^i\right), \\ \boldsymbol{q}_j^2 &= \boldsymbol{k}_j'^f - \boldsymbol{k}_j^i = (\boldsymbol{q}_\parallel, q_{z,j}^2) = \left(\boldsymbol{q}_\parallel, -k_{z,j}^f - k_{z,j}^i\right), \\ \boldsymbol{q}_j^3 &= \boldsymbol{k}_j^f - \boldsymbol{k}_j'^i = (\boldsymbol{q}_\parallel, q_{z,j}^3) = (\boldsymbol{q}_\parallel, -q_{z,j}^2), \\ \boldsymbol{q}_j^4 &= \boldsymbol{k}_j'^f - \boldsymbol{k}_j'^i = (\boldsymbol{q}_\parallel, q_{z,j}^4) = (\boldsymbol{q}_\parallel, -q_{z,j}^1). \end{aligned} \tag{14}$$

Here, $\boldsymbol{q}_\parallel$ is the in-plane component of the wave vector transfer, which is identical throughout the whole film in order to fulfill the boundary conditions. The four wave vector transfers arise from the cross product of the two eigenstates in Eqs. (5) and (6), as schematically shown in Fig. 2. They can also be understood as four scattering events distinguished by different combinations of the reflection and refraction,[10,29,30] with each event weighted by a corresponding coefficient given in Eqs. (13).

Usually a local monodisperse approximation[43] is applied, where each nanostructure is assumed to be surrounded by others of identical shape and the scattering intensity arises from the incoherent sum of the scattering from monodisperse regions weighted by the nanostructure size distribution $\mathcal{N}(\boldsymbol{R})$. If the film is treated as a single layer and the incident angle is sufficiently large so that $R^i = R^f = 0$, and $T^i = T^f = 1$, the diffuse cross section (Eq. 12) simply reduces to

$$\left(\frac{d\sigma}{d\Omega}\right)_{\text{diff}} \approx r_e^2 \left|\Delta\rho\right|^2 \left\langle \left|F(\boldsymbol{q},\boldsymbol{R})\right|^2 \right\rangle_{\mathcal{N}(\boldsymbol{R})} \left|S(\boldsymbol{q})\right|^2, \tag{15}$$

where $F(\boldsymbol{q},\boldsymbol{R})$ is the stand-alone form factor of the nanostructure of size dimension $\boldsymbol{R}$. The above equation is essentially the Born approximation (BA).

We now make an assumption that the scatterings from the jth and lth layers ($j \neq l$) do not have phase relation so that the cross terms in Eq. (12) cancel out on average. Noticing that the in-plane area illuminated in a grazing-incidence geometry over which the average is performed is much larger than the area of the incident beam coherent volume, the above assumption is generally valid if the absolute nanostructure distributions between these two layers are spatially uncorrelated. Within each coherent area, the in-plane correlation is accounted for by the structure factor. The diffuse part of the differential cross section can then be approximated by

$$\left(\frac{d\sigma}{d\Omega}\right)_{\text{diff}} \approx r_e^2 \sum_{j=1}^{N+1} \Delta\rho_j \Delta\rho_j^* \sum_{m,n=1}^{4} D_j^m D_j^{n*} S_j(q_{z,j}^m, \boldsymbol{q}_\parallel) S_j^*(q_{z,j}^n, \boldsymbol{q}_\parallel) \left\langle F_j(q_{z,j}^m, \boldsymbol{q}_\parallel, \boldsymbol{R}) F_j^*(q_{z,j}^n, \boldsymbol{q}_\parallel, \boldsymbol{R}) \right\rangle_{\mathcal{N}(\boldsymbol{R})}. \tag{16}$$

Here, the depth sensitivity is intrinsically built-in in the multilayer DWBA theory as a depth-dependent summation when a nonuniform EFI distribution is present in the sample. If the EFI is treated as an invariant, this depth sensitivity vanishes. It then leads to the expression of the conventional single-layer DWBA theory,[10,29] where the electron density of the film is treated homogenously and the distortion of the EFI arising from the nanostructures is not taken account into the unperturbed term for the DWBA calculations. However, the contribution from the nanostructures to the EFI is automatically included in the current developed multilayer theory, similar to the self-consistent DWBA theory for low-intensity neutron scattering from rough surfaces at grazing incidence.[44]

In certain cases where the interlayer structures are spatially correlated, for example, in the study of the vertical topological replication of nanoparticle monolayers in multilayer nanocomposite films,[7] the roughness correlations were obtained right from the cross product terms in Eq. (12). Another situation when these cross terms cannot be neglected is the presence of large nanoparticles in a significantly varying EFI distribution. The nanoparticle has to be discretized into multilayer disks, but the lateral positions of these disks are aligned uniaxially, i.e., completely correlated in the vertical direction. This correlation gives the vertical shape of the nanoparticle, and it can only be expressed by the cross terms, which will be discussed in detail below.

B. X-ray standing wave effect

To understand how the depth sensitivity of the XSW comes into the calculation of the GISAXS differential cross section, we will use the XSW generated above a flat Ag mirror in air as an example. Assuming an incident x-ray energy of 8.04 keV (throughout the rest of the paper), the calculated EFI (defined as $\left|\psi^i(z)\right|^2$) as a function of distance from the mirror surface is shown in Fig. 3. Higher incident angles, but still below the Ag critical angle α_c^{Ag} ($= 0.44°$), create more EFI oscillations than low incident angles. Let's consider how nanoparticles at different heights above the mirror surface contribute to the total scattering. The two particles shown in Fig. 3 experience a similar EFI on average when the incident angle α^i is large, e.g., close to α_c^{Ag}. However, for a smaller angle of $\alpha^i = 0.08\alpha_c^{\text{Ag}}$, particle A suspended at ~ 60 nm above the substrate coincides with the antinode of a maximum EFI, while particle B suspended at ~ 125 nm coincides with the node of a minimum EFI. As a result, the scatterings from particles at different heights cannot be added with an equal weight. Instead, they have to be weighted by coefficients given in Eqs. (13). In addition, in case that the nanoparticle size is much larger than the EFI variation pattern (e.g., for $\alpha^i = \alpha_c^{\text{Ag}}$) so that the particle is not exposed to a uniform electric field, it cannot be treated as a conventional single particle with a full form factor, as in transmission small-angle x-ray scattering, unless the variations of the particle shape and density distribution is far

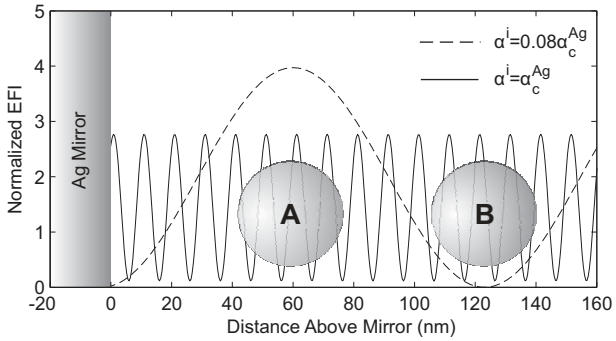

FIG. 3. Calculated EFI profiles extended on a silver mirror in air for two incident angles.

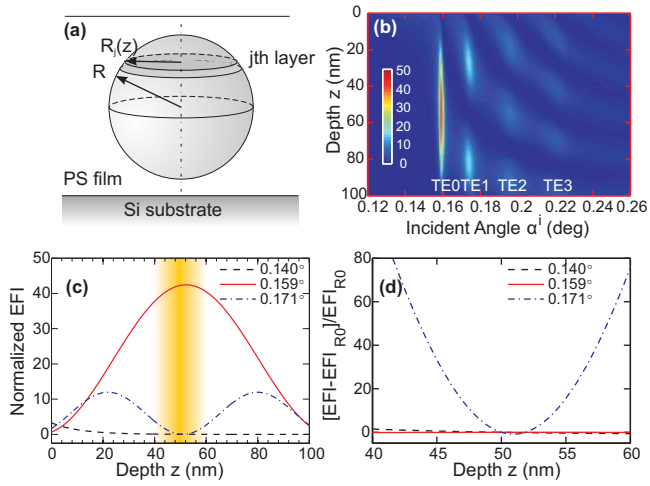

FIG. 4. (a) Schematic of the slicing of a spherical nanoparticle buried at the middle of a Si-supported polystyrene film. Particle size is not drawn to scale. (b) Normalized EFI plotted as a 2D map as a function of incident angle and film depth. (c) EFIs for three incident angles. The shadow region corresponds to the location of the nanoparticle. (d) EFIs at the particle region [shadow in (c)] re-scaled to EFI($z = d/2$).

less than the variation of the EFI pattern (e.g., a uniform cylinder normal to the surface spans across the entire film). Therefore, special care has to be taken into account when the standing wave effect cannot be neglected. Although the calculation of the differential cross section becomes sophisticated and demands more computing time, the benefit of this effect is that one can take advantage of the resonance-enhanced scattering to gather depth-dependent information of the nanostructures, such as the shape of the nanoparticles and the packing motifs at various depths. Also note that the presence of nanostructures, especially densely packed heavy metal nanoparticles, may induce significant perturbations to the electric field distribution.[5,6] In this case, the unperturbed state has to be redefined in a manner such that the mean electron density of each layer is calculated with the contribution of the nanoparticles taken into account, in full or in part, as discussed in Section II A.

C. Form factor

As we have discussed in section II B, in many cases, a single large nanoparticle cannot be treated as a single object with a conventional full form factor expression due to the generation of the standing wave. To illustrate how different parts of such a nanoparticle unevenly contribute to the total scattering, we consider spherical nanoparticles of radius R as an example. As shown in Fig. 4a, a nanoparticle is divided into a stack of disks with depth-dependent radii. Hence, the form factor in the jth layer is simply the in-plane component of a cylinder's form factor

$$F_j(q_\parallel, q_z) = 2\pi R_j^2 d_j \frac{J_1(q_\parallel R_j)}{q_\parallel R_j} e^{iq_z d_j/2}, \tag{17}$$

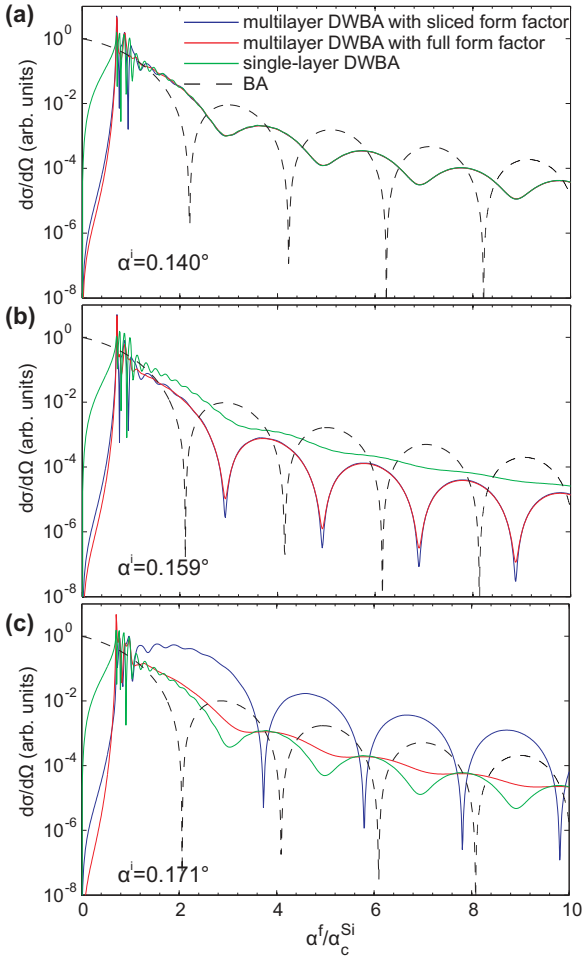

FIG. 5. Calculated differential cross sections at an incident angle of (a) 0.140°, (b) 0.159°, and (c) 0.171°, respectively, using four models described in the text for a gold nanoparticles buried at the middle of a Si-supported polystyrene film. The curves are shifted vertically for a better comparison.

where R_j and d_j are the radius and thickness of the disk in the jth layer, and J_1 is the Bessel function of the first kind. A depth integral of Eq. (17) gives the conventional form factor of a full sphere

$$F(q) = \sum_j F_j(q_\parallel, q_z) = 4\pi R^3 \frac{\sin(qR) - qR\cos(qR)}{(qR)^3} e^{iq_z R}. \tag{18}$$

This slicing method for the form factor can be readily generalized to anisotropic nanoparticles of other shapes.[31] One can still use the conventional form factor for very small nanoparticles so long as their shape and density do not vary significantly along the surface normal when compared with the variation of the electric field. However, once this slicing method is used in the presence of large particles, the phases of the scattering from coherent regions across the layers cutting the same particle are no longer independent on average. As a consequence, this invalidates Eq. (16). Instead, the full expression in Eq. (12) has to be used to calculate the differential cross section.

To further understand the slicing method, we consider a spherical gold nanoparticle of radius $R = 10$ nm buried at the middle ($d/2$) of a Si-supported polystyrene (PS) film of thickness $d = 100$ nm (Fig. 4a). Critical angles for Si and PS at $E = 8.04$ keV are $\alpha_c^{\rm Si} = 0.224°$ and $\alpha_c^{\rm ps} = 0.154°$, respectively. The normalized EFI map is shown in Fig. 4b. Four resonant angles can be seen between the two critical angles: 0.159°, 0.174°, 0.195°, and 0.220°, which are assigned as $\rm TE_0$-$\rm TE_3$, respectively. The corresponding 1D EFI profile is displayed in Fig. 4c for $\alpha^i = 0.140°$ below $\alpha_c^{\rm ps}$, 0.159° where, at $z = d/2$, the EFI reaches its local maximum (antinode), and 0.171° where, at $z = d/2$, the EFI is nearly minimum (node). At 0.159°, the EFI is significantly enhanced by a factor of ~ 45 in the middle of the film, while the EFI at the surface is nearly zero. In order to view how different depths of the nanoparticle are subject to the variation of the EFI, a rescaled EFI is plotted in Fig. 4d with respect to the EFI value at the center plane of the nanoparticle, $z = d/2$. Figure 5 shows differential cross sections calculated for these incident angles in the scattering

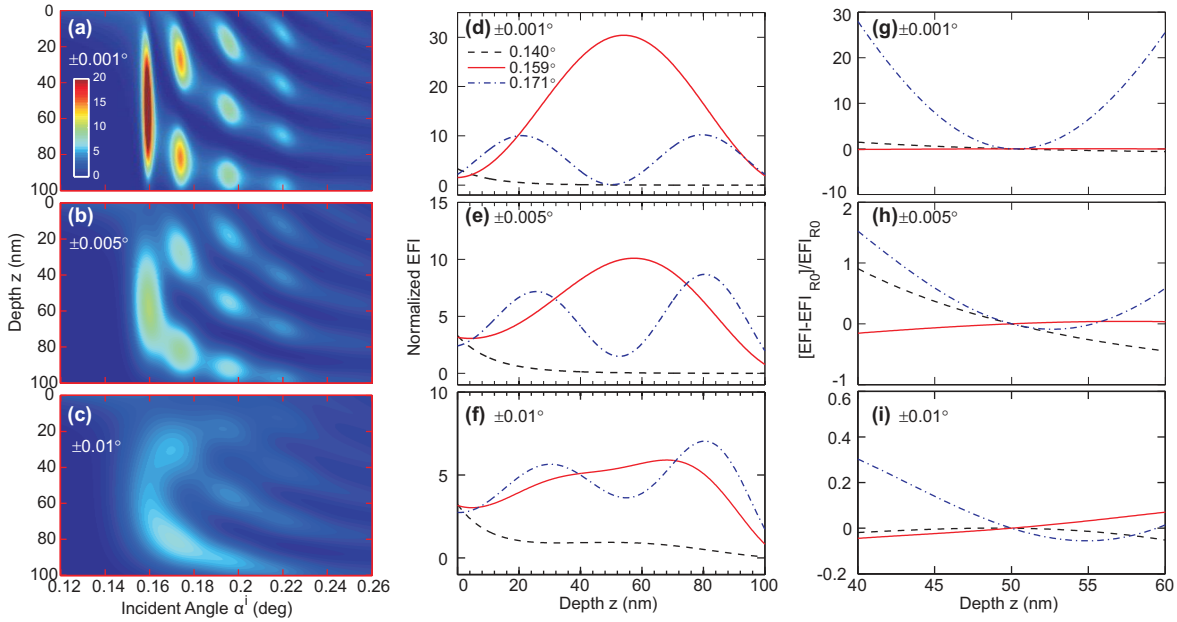

FIG. 6. (a-c) Calculated normalized EFI with an incident beam divergence 0.001°, 0.005°, and 0.01° for the sample shown in Fig. 4a. (d-f) Corresponding EFI profile for three incident angles, 0.140°, 0.159°, and 0.171°. (g-i) EFIs rescaled to the EFI value at $z = d/2$.

plane ($\chi = 0$) using four different models: multilayer DWBA with sliced form factor by Eq. (12), multilayer DWBA with full form factor by Eq. (16), single-layer DWBA that is widely used but treats the film as a single layer without depth-dependence and resonant effect considered,[10,12,29–31] and BA by Eq. (15). At 0.140° below the film critical angle, evanescent waves are created underneath the surface, and the EFI decays exponentially as depth increases. The EFI varies very slightly across the nanoparticle (Fig. 4d), and both multilayer DWBA models (with sliced and full form factors), as well as the single-layer DWBA, yield nearly identical results except at near the critical angle where the fringes differ in both phase and amplitudes (Fig. 5a). This is ascribed to the significant angle-dependent T^f and R^f on the exit side of the scattering near the critical angle. Note that, although the overall scattering intensity is determined by the EFI from the incident side, T^f and R^f for the exit sides also affect the scattering as they come into the differential cross section (Eq. 13). The same argument applies to the scattering at the resonant angle 0.159°, where the EFI hardly varies through the nanoparticle (Fig. 4c) and thus both multilayer DWBA models give nearly identical results (Fig. 5b). However, the cross section by the single-layer DWBA is significantly different, because it assumes an invariant EFI throughout the film and neglects the inhomogeneity nature of the nanostructure along the direction normal to the surface. Complex coefficients T^i and R^i calculated by the single-layer DWBA are nearly out of the phase so that it smears the fringes. At 0.171°, a major part of the nanoparticle in its center does not see the x-ray, and the EFI distribution varies drastically so that one cannot calculate the cross section using a conventional full form factor any more. This example indicates that the electric field pattern varies significantly with the incident angle, and only if the variation of the electric field pattern is far less than that of the nanostructure of interest, can one employ the full form factor. Otherwise, the concept of the conventional form factor is invalid and a slicing method has to be used.

D. Resolution effect

In Fig. 4b, we notice that the resonant angles (TE_0-TE_3) are very close, especially for lower TE modes because of refraction effect. This implies that the beam divergence has to be sufficiently small so as to distinguish these modes. To quantify such resolution effect, we recalculated the EFI distribution map by an incoherent convolution with a Gaussian incident beam of a divergence width of 0.001°, 0.005°, and 0.01° (Fig. 6a-c, respectively). As the beam divergence gradually increases, the EFI gets smeared first at the low-incident-angle region. This is because unlike a reflectivity above the substrate critical angle whose Kiessig fringes are uniformly spaced in angle, the spacing between resonant angles is not even and is more compact at low angles. Therefore, when the divergence increases to 0.005°, the 1st and 2nd resonant angles first start to smear and merge. As the divergence increases to 0.01°, the EFI differs

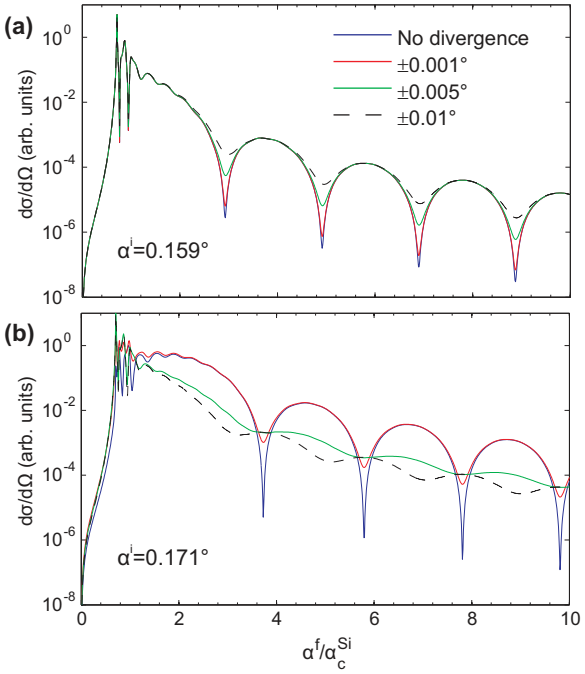

FIG. 7. Effect of the incident beam divergence on the differential cross section at a nominal incident angle of (a) 0.159°, and (b) 0.171°, using the multilayer DWBA model with sliced form factor.

significantly from the original high-resolution one. Corresponding EFI line profiles for the three incident angles are displayed in Fig. 6d-f, respectively. The values of the EFI profile at the resonant angle (0.159°) is the most affected by the resolution effect, i.e., the enhancement at the peak is greatly reduced compared with that for a nondivergent beam. A divergent incident angle leads to a divergent exit angle. A simple scattering geometry for a flat surface at grazing-incidence angles implies that the exit-angle divergence depends on the footprint size. Therefore, it varies at different exit angles and also depends on the sample-to-detector distance and the out-of-scattering-plane angle. When calculating the differential cross section, the divergences for both the incidence and exit beams have to be convoluted with the product of the D_j^m coefficients and the form factor (either sliced or conventional full expressions). For exit angles much larger than the substrate critical angle, the exit beam divergence hardly affects T^f and R^f coefficients because $T^f \approx 1$ and $R^f \approx 0$ and can then be negligible. A strict treatment of the resolution effect involves a consideration of the mutual coherence functions of the beam, as well as the electron density distribution of the sample,[45] which is beyond the scope of this work. However, in order to study the extent to which the buried nanostructures can be determined in the presence of a smeared EFI distribution due to incident beam divergence, we simply neglect the exit beam divergence. Figure 7 shows the recalculated differential cross sections using the multilayer DWBA model with sliced form factor given by Eq. (12). At a nominal incident angle of 0.159°, although the EFI values at the nanoparticle position dropped significantly with an increase in the divergence, the EFI distribution is still nearly flat across the nanoparticle (Fig. 6g-i). This implies that the divergence mostly affects the convolution with the form factor, in a manner similar to how the nanoparticle polydispersity contributes, i.e., yielding a smearing of the oscillation amplitudes (Fig. 7a). However, the effect due to the incident beam divergence is very different at a nominal incident angle 0.171°, where the EFI distribution across at the nanoparticle region significantly varies (Fig. 6g-h), especially for the divergence larger than 0.005°. This leads to a differential cross section with not only smeared oscillation amplitudes but also shifted oscillation positions (Fig. 7b). This example, from the resolution aspect, also indicates that the depth-dependent EFI distribution is critical for the calculation of the scattering intensity from buried nanostructures, especially when the dimensions of these structures are comparable or beyond the EFI variation patterns.

In addition to the beam divergence, any factor that changes the EFI distribution except the nanostructure of interest contributes to the overall resolution, e.g., the pixel resolution of the detector, macroscopic flatness of the sample and even the sample roughness. Approximately, the detector resolution can be taken into account by a convolution with the pixel solid angle for the final scattering intensity; the flatness is included equivalently as the beam divergence; and the surface roughness is treated with the effective-density model[41], where the near-surface region is reduced to small independent layers prior to the calculation of the EFI distribution. Distinguishable XSWs in films can only be

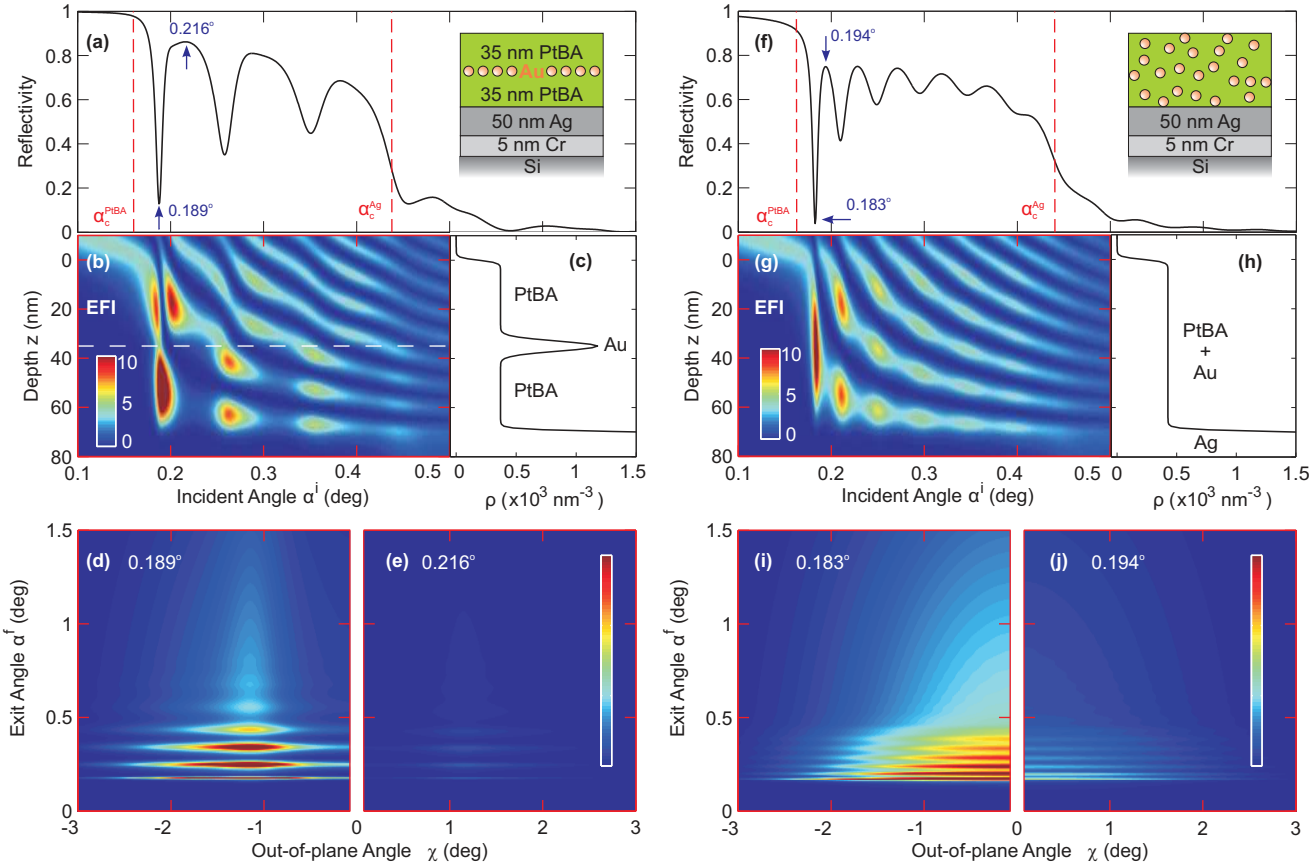

FIG. 8. (a) and (b) are the reflectivity and the normalized EFI for a sandwiched film schematically shown in the inset of (a). The critical angles for PtBA and Ag are shown as red dot lines in (a). The white dot line in (b) indicates the position of the Au nanoparticle monolayer. (c) The electron density profile normal to the surface. (d) and (e) The calculated GISAXS patterns with incident angle at the first resonant angle and a nonresonant angle marked by arrows in (a). (f)-(j) The same film but with the Au nanoparticles evenly dispersed throughout the PtBA layer.

generated by a beam of high resolution. This can be readily achieved on typical instruments at the third-generation synchrotron radiation sources, such as beamline 8-ID at the Advanced Photon Source (APS). For this reason, the resolution effect is not of a concern in the following discussion.

III. CASE STUDIES

A. Nanoparticle-polymer composite films

We now demonstrate how the standing wave effect can be applied in combination with GISAXS to facilitate uncovering buried nanostructures. Inspired by a recent pioneering experimental work of applying a thin-film-based x-ray waveguide technique to study the ordering kinetics and dynamics in a nanoparticle-polymer nanocomposite,[5,6] we consider a representative sample as shown in Fig. 8a, where a monolayer of Au spherical nanoparticles of radius $R = 1.75$ nm is sandwiched between two layers of poly(*tert*-butyl acrylate) (PtBA) of equal thickness of 35 nm. The nominal thickness of the nanoparticles is assumed to be 1 nm, which is the equivalent thickness for a continuous Au monolayer. The depth distribution of the nanoparticles is assumed to be Gaussian with a width of 2 nm. A 50-nm-thick Ag mirror of high electron density is used as the substrate, which sits on a Si substrate coated with 5 nm Cr. Identical roughness of 1 nm is assumed for each interface. The electron density distribution is then calculated and shown in Fig. 8c. The position distribution of these nanoparticles is assumed to be isotropic in the monolayer plane, and a 1D paracrystal model[46,47] is then applied to describe this distribution. By assuming a Gaussian probability distribution function for the positions $p(r) = \left(1/\sqrt{2\pi\sigma_d^2}\right) e^{-(r-d)^2/2\sigma_d^2}$, where $d = 6.5$ nm is the nearest-neighbor

distance and $\sigma_d = 2.5$ nm is its root-mean-square deviation, the modulus square of the structure factor is given by[48]

$$\left|S(q_\parallel, q_z)\right|^2 = \frac{1 - e^{-q_\parallel^2 \sigma_d^2}}{1 + e^{-q_\parallel^2 \sigma_d^2} - 2e^{-q_\parallel^2 \sigma_d^2/2} \cos(q_\parallel d)}. \tag{19}$$

The reflectivity and the normalized EFI are calculated by Parratt's recursion[36,40,41] and are shown in Figs. 8a and 8b, respectively. Three resonance modes exist between the critical angles of PtBA and Ag. Because the nanoparticle size is very small compared with the electric field variation pattern, Eq. (16) is used to calculate the GISAXS patterns at the first resonant angle and a nonresonant angle (Fig. 8d and 8e). At the resonant angle, the scattering intensity can be seen to be significantly enhanced compared with that at the nonresonant angle. Therefore, although the depth-dependent structure is self-contained partially in the angle dependent T^f and R^f on the exit side of the scattering, it can be determined to a much better accuracy with an increased signal-to-noise ratio by tuning the incident angle to selectively illuminate buried morphology at a certain depth level. This standing-wave-based technique has successfully been applied in combination with *in situ* GISAXS to measure the lateral and normal diffusion coefficients of the Au nanoparticles during thermal annealing.[5,6]

We now consider a film with the monolayer of Au nanoparticles diffused evenly throughout the PtBA film (Fig. 8f inset). The PercusYevick hard-sphere approximation[49] is used for the structure factor[43,50]

$$\left|S(q_\parallel, q_z)\right|^2 = \frac{1}{1 + 24\eta G(2qR)/(2qR)}, \tag{20}$$

where η is the volume fraction of the nanoparticles, and

$$\begin{aligned}
G(x) &= \frac{\alpha}{x^2}(\sin x - x\cos x) \\
&+ \frac{\beta}{x^3}\left[2x\sin x + (2 - x^2)\cos x - 2\right] \\
&+ \frac{\gamma}{x^5}\{-x^4\cos x + 4\left[(3x^2 - 6)\cos x + (x^3 - 6x)\sin x + 6\right]\}, \\
\alpha &= (1 + 2\eta)^2/(1 - \eta)^4, \\
\beta &= -6\eta(1 + \eta/2)^2/(1 - \eta)^4, \\
\gamma &= \eta\alpha/2.
\end{aligned} \tag{21}$$

This monodisperse hard-sphere model has been used to analyze GISAXS data from nanoporous films.[10,51] The reflectivity and EFI for the nanoparticle dispersed film are shown Figs. 8f and 8g. Instead of three, six resonance modes are observed, because the electron density along the surface normal is now more uniform across the entire film thickness (Fig. 8h) and the homogenous film thickness is doubled. The GISAXS patterns at the first resonant and a nonresonant angles are shown in Figs. 8i and 8j, respectively. The intensity contrast between these two angles is less prominent than that for the sandwiched film because there are many more nanoparticles still in the illumination at nonresonant angles.

The synergistic interactions between inorganic self-organizing particles and a self-assembling matrix of organic or biological templates have been shown to be able to induce cooperative, coupled self-assembly and thus produce hierarchically ordered structures.[19,52] As an ideal nondestructive and depth-sensitive surface probe, GISAXS is often widely used to characterize films of these complex nanocomposites composed of inorganic nanoparticles and self-assembled block copolymers. Here, for an example, we focus on a typical model system of a 100-nm silicon-supported nanocomposite film of polystyrene-*block*-poly(2-vinylpyridine) (PS-*b*-P2VP) mixed with spherical CdSe nanoparticles ($R = 2$ nm). Assume the diblock copolymer can self-assemble into cylinder microdomains ($R_C = 10$ nm). The segregation of the nanoparticles onto the surface mediates the interfacial interactions and thus may direct these hexagonally packed microdomains normal to the substrate that otherwise would be parallel without the presence of nanoparticles.[19,53] The structure of the cylinder lattice can be described either by a finite-sized regular bidimensional lattice or by the bidimensional paracrystal theory,[31,54] the latter being used to model the cylinder hexagonal lattice in the present,

$$S_{\text{hex}}(q_\parallel) = \prod_{k=a,b} \text{Real}\left[\frac{1 + P_k(q_\parallel)}{1 + P_k(q_\parallel)}\right], \tag{22}$$

where $P_k(q_\parallel) = \exp(-q_{\parallel,k}^2 \sigma_D^2/2)\exp(iq_{\parallel,k}D)\exp(-D/\Lambda_0)$ is the Fourier transform of the probability density of finding a P2VP cylinder at a distance of $D = 36$ nm along the base axes a and b of the hexagonal unit cell, assuming that a and

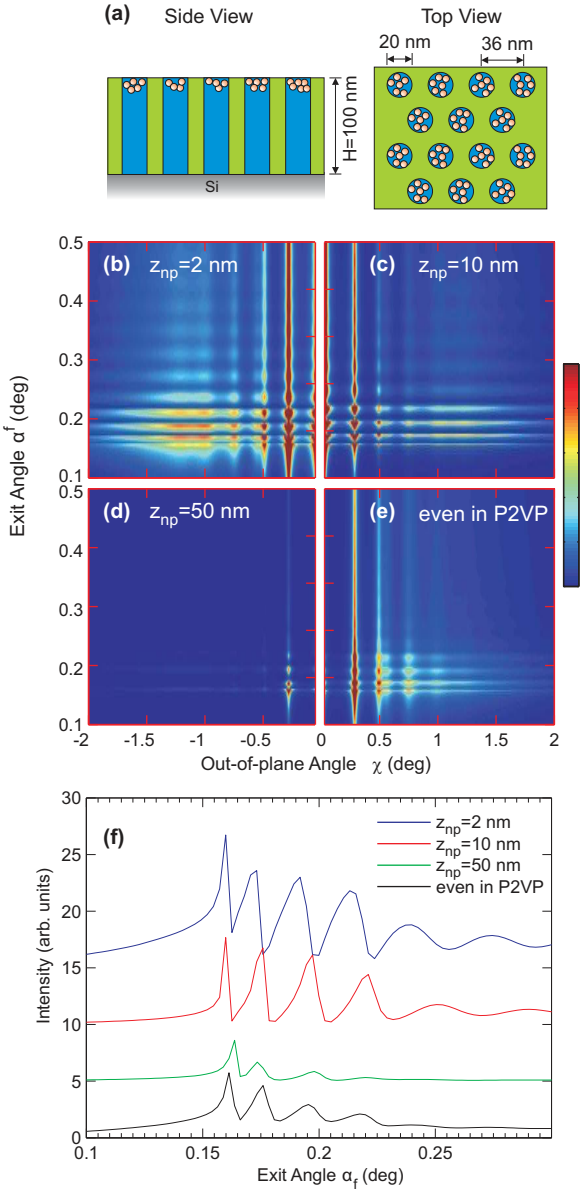

FIG. 9. (a) Schematic of the nanoparticle-block copolymer composite film. (b) and (c) Calculated GISAXS patterns at a grazing-incidence angle of 0.15° when the depth of the nanoparticles is at $z_{\rm np}$ = 2 nm, 10 nm, 50 nm and evenly distributed in P2PV, respectively. (d) Comparison of the vertical linecuts along the (10) diffractions.

b directions are independent. Here a Gaussian probability distribution is used with a standard deviation $\sigma_D = 3.6$ nm. To account for the finite size effects, $\Lambda_0 = 100D$ is introduced as a correlation length. The nanoparticles prefer P2VP domains and are assembled on the top of each P2VP cylinder domain into a relatively disordered packing that can be modeled using Eq. (19), as shown in Fig. 9a. Four depth locations of the nanoparticles are used to calculate the GISAXS patterns, $z_{\rm np}$ = 2 nm, 10 nm, 50 nm with a Gaussian depth spread of 2 nm and evenly distributed in the P2VP cylinder. Usually within the x-ray footprint at a grazing-incidence angle, hexagonal domains of various orientations exist. Therefore, an in-plane (parallel to surface) angular average (2D powder diffraction) is performed during the calculation of the GISAXS pattern. Diffractions corresponding to the (10), (11), (20) and higher orders of the 2D hexagonal lattices can be seen in Figs. 9b-e. The broad peak at the large out-of-scattering-plane angle χ in Fig. 9b-d corresponds to the interparticle correlation of the nanoparticles. From the GISAXS pattern, a highest overall intensity for the $z_{\rm np}$ = 2 nm film is observed as compared to films of other nanoparticle distributions due to the strongest EFI close to the surface at the incident angle of 0.15°. The XSW fringes near the critical angles significantly differ from each each for different films, as shown in Fig. 9f. For example, the XSWs antinode (peak and dip) positions and symmetries are very different; the XSW antinode envelopes decay differently as the exit angle

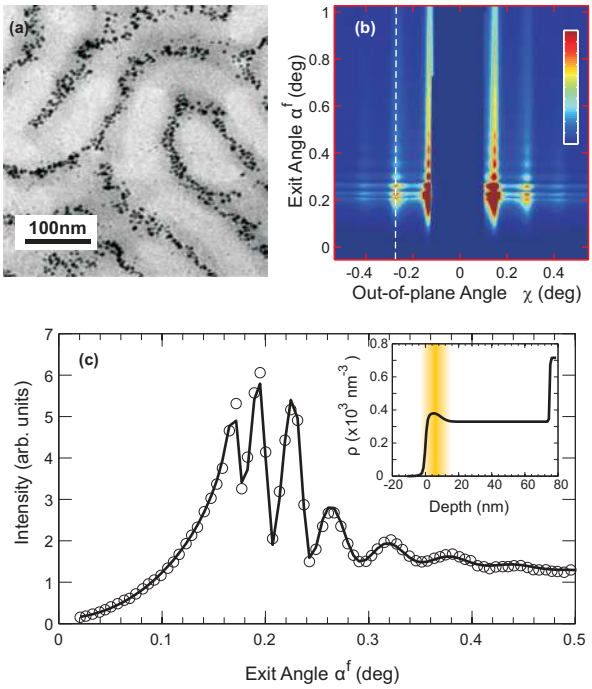

FIG. 10. (a) TEM image of the nanoparticle-polymer composite film after solvent and thermal annealing. (b) GISAXS pattern taken with x-rays of energy 7.35 keV at an incident angle of 0.18°. (c) Circles correspond to the vertical linecut along the (20) lamellar diffraction peak marked by the dotted line in (b). Solid line is the best fit to the model described in the text. Inset is the fitted electron density profile showing an aggregation of nanoparticles near the surface (shadow region).

increases; the intensity rises most steeply for the $z_{\rm np} = 50$ nm film as the exit angle approaches the first resonant angle value. All these features prove XSW a very sensitive probe to determine the depth location of the nanoparticles. Therefore, by a quantitative analysis of the experimental GISAXS data, detailed complex film structures at various levels of length scales, such as the nanoparticle location, packing parameters, as well as the cylinder lattice parameters, can be obtained. Presented below is an experimental application of how to use the high sensitivity of the XSW to determine the nanoparticle distribution in a nanoparticle-polymer composite film.

A ∼75-nm-thick composite film of gold nanoparticles ($R = 2.15$ nm) and lamella forming PS-*b*-P2VP diblock copolymers was made. After a solvent annealing followed by a thermal annealing, gold nanoparticles migrated into the P2VP phase of the vertical lamellar structures.[55] Figure 10a shows the TEM image of the film. Figure 10b is the GISAXS pattern, where the diffractions from lamellae normal to the surface can be seen. The XSW oscillations arising from the strong wave-guide effect are also observed near the critical angles of the film and the substrate. The presence of the nanoparticles should significantly change the electron density profile in the film and thus the XSW oscillations. In order to determine the nanoparticle depth distribution, a linecut along the (20) order diffraction is fitted to the multilayer DWBA theory described in Eq. (16). Extremely good fitting to the XSW oscillations is obtained, and it is found that, after both solvent and thermal annealing, the nanoparticles aggregate to a layer at 4.9 nm below the surface with a Gaussian distribution width of 4.2 nm. This example demonstrates that a close quantitative examination of the XSW near the critical angles can give very rich information of the buried nanostructures, which, however, is often neglected in conventional GISAXS analysis.

B. Block copolymer films

Self-assembly of block copolymer films often produce ordered nanostructures of sizes up to tens to hundreds of nanometers across the whole film. At grazing-incidence angles, these nanostructures are exposed to different electric fields at different depths. Therefore, a slicing of the nanostructure has to be applied when calculating the GISAXS intensity. This point is now illustrated by an experimental example from a spun-cast 41-nm-thick PS-*b*-P2VP film on a lithographically patterned silicon substrate with hexagonal wells. Figure 11a shows the SEM image of the substrate. The registration of the block copolymer to the patterned substrate leads a monolayer of highly ordered P2VP micelles (R =8 nm) that align with the well walls.[56] This monolayer with micelles separated at an interparticle distance of

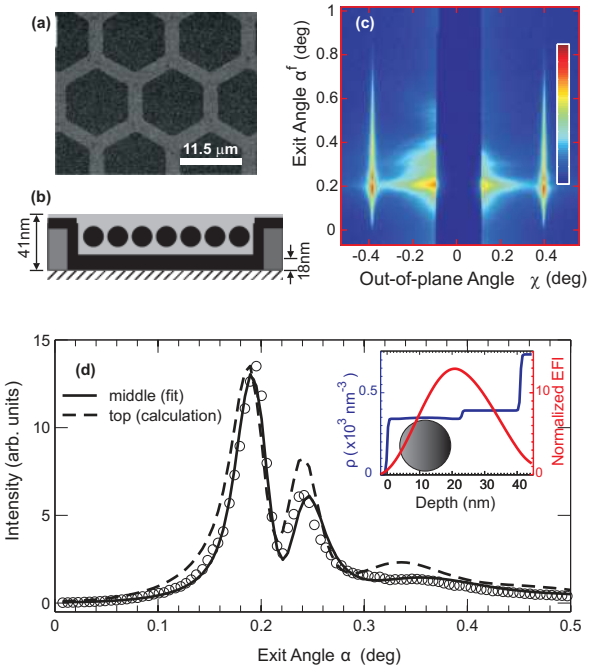

FIG. 11. SEM image of a hexagonally patterned silicon substrate. (b) Schematic of the ordered embedded P2VP micellar monolayer within in a well defined by the pattern. (c) GISAXS image at an incident angle of 0.195°. (d) Circles correspond to the vertical linecut along the (10) micellar diffraction peak. Solid line is the best fit to the model described in the text with the micellar center located at a depth of 11.9 nm, near the middle of the PS matrix film. Dashed line the calculated values assuming the depth of the micellar center is 8 nm, near the top of the PS film. Inset is fitted electron density profile and corresponding normalized EFI at 0.195°.

28.1 nm is embedded within the PS matrix of thickness 23 nm, which sits on a 18-nm-thick P2VP brush cushion formed from the partial wetting of P2VP to the substrate. The GISAXS (Fig. 11c) was taken at 7.445 keV at an incident angle of 0.195°, where standing wave oscillations are clearly seen near the critical angles of the film and the substrate. Very strong (10) diffraction peaks arise from the intermicelle correlation. A vertical linecut along the (10) diffraction is analyzed for the position of the P2VP micellar monolayer, as shown in Fig. 11d. The scattering from the walls of the substrate can be neglected because the well width is 11.5 μm, far beyond the length scale of the micellar separating distances. Because of the large size of the micelles, a slicing of the micellar shape, similar to the method in II C, has to be used to model the form factor. Fitting to the multilayer DWBA theory with a sliced form factor yields a remarkably good agreement with the experiment data especially near the XSW resonant oscillations, indicating that the monolayer of the P2VP micelles is located at a depth of 11.9 nm, nearly at the center of the PS matrix. The XSW oscillations are very sensitive to the micellar position. For example, if one assumes the micelles are embedded near the surface at a depth of 8 nm, the calculated intensity profile (dashed line in Fig. 11d) shows very different XSW peak positions and relative peak intensities. Therefore, very rich information regarding to the depth of the nanostructures can be obtained with a nanometer or even subnanometer spatial resolution by analyzing XSW profile in the region near the critical angles.

C. Supported nano-objects

We now discuss how the discretized multilayer DWBA theory developed here for general purposes can be applied to calculate the GISAXS from supported nano-objects. For small isolated objects with very low surface coverage, the electric field distribution extended above the substrate is not significantly altered, and the objects are exposed to a nearly uniform electric field so that the conventional island DWBA theory[22,23,30,31] applies to GISAXS without much problem. However, this theory gives large deviations when the nano-object is subject to a nonuniform field that varies in a pattern that is comparable to the object size. This may occur in one or more than one of the following situations: very low incident angle, object size comparable to the electric field variation pattern, and large perturbations to the electric field arising from large surface concentration of the nano-objects.

Assume Si-supported Ge nanoislands of truncated square pyramid (Fig. 12a inset), a typical shape for the self-

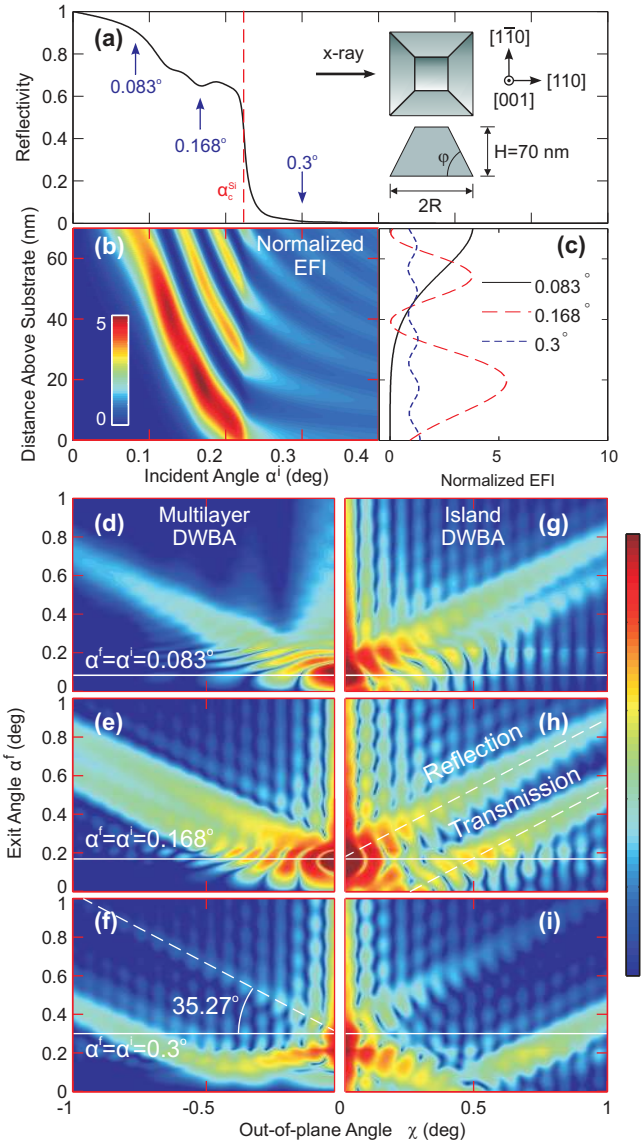

FIG. 12. (a) and (b) Reflectivity and normalized EFI for Si-supported Ge nanoislands of dimensions displayed in the inset in (a). The arrows in (a) indicate the three incident angles for GISAXS calculations, with corresponding EFIs shown in (c). (d)-(f) and (g)-(i) Calculated GISAXS patterns using the multilayer DWBA and island DWBA theories described in the text, respectively.

organized mesoscopic semiconductor structures.[25,57] The dimensions of the pyramid are chosen so that the ratio of the base width to the height is $2R/H = 1.96$ and the facet angle between (111) and (001) planes is $\varphi = 54.73$. This shape and dimension is energetically favored because of the minimized surface-to-volume ratio. A surface occupation of 30% (fraction of the total pyramid base area) is used so that the electric field is perceptibly perturbed. For a better understanding of the interference bewteen EFI and the shape of the nano-objects, the in-plane interparticle correlation is dropped (which can be included easily as described in the paper). X-rays of 8.04 keV are incident along the [110] direction parallel to the base edge. From the reflectivity (Fig. 12a) and the EFI (Fig. 12b), weak resonance modes are established, and the electric field is altered significantly from that on an unperturbed bare Si substrate, especially for $\alpha^i < \alpha_c^{\rm Si}$. The GISAXS pattern is simulated at three incident angles using both the multilayer DWBA theory and the conventional island DWBA theory. The island DWBA yields a GISAXS pattern with two significant scattering sets with one assigned to the transmission branch centered at the direct beam position and the other one assigned to the reflection branch centered at the specular position, as shown in Figs. 12g-i. These two branches merge at $\alpha^i = 0$ and become clearly separated as α^i increases.[28] However, in the picture of the multilayer DWBA, a single object is decomposed into a stack of disks, the scatterings from which are summed up coherently. While our theory

also yields two scattering branches, it presents a significant difference from the island DWBA theory, especially at a small α^i. In Fig. 12d for $\alpha^i = 0.083°$, the two branches are totally mixed, and much fewer number of fringes are observed with a larger periodicity when compared with the island DWBA result in Fig. 12g. This is because, at this grazing angle, the form factor of the pyramid is truncated by an EFI that monotonically decays upon the depth. Only the topmost portion of the pyramid is illuminated (Fig. 12c), which effectively resembles a pyramid of a smaller size. The discrepancy between these two theories decreases as α^i increases. At $\alpha^i > \alpha_c^{\mathrm{Si}}$, the positions of the two scattering branches predicted by the two theories are nearly identical. However, the intensity of the reflection branch calculated by the multilayer DWBA is much weaker than that by the island DWBA. This is ascribed to the high surface concentration of the nanoislands, which greatly suppresses the reflection by the substrate.

In addition, using the discretized multilayer DWBA one may be able to obtain the internal density of the islands normal to the surface if a depth-dependent electron density profile for the island is applied to model the GISAXS pattern. Therefore, it may provide an alternative method to perform electron density reconstruction of supported nano-objects, which is now usually performed by combining the coherent GISAXS and the tomographic phase retrieval methods.[27,28]

IV. CONCLUSIONS

We have derived the Parratt-formalism-analog of the diffuse scattering differential cross section in the context of the multilayer DWBA to treat GISAXS problems, especially in buried layers with waveguide enhancement and when the nanostructure size is comparable to the EFI spatial period. In this theory, the electric field intensity for the unperturbed state is calculated with the distortion from the nanostructure of interest taken into account in a self-consistent fashion. In addition, the kinematic form factor used in conventional DWBA theories has to be replaced with a coherent integration of the discretized "form factor" multiplied by corresponding electric field. Such layered analysis is only valid when the beam resolution is high enough so that XSW modes can be well distinguished. With the current theory applied to the GISAXS at various grazing angles where x-ray standing wave changes locations, one can obtain quantitative information about the depth-dependence of the buried nanostructures.

ACKNOWLEDGMENTS

This work is supported by the U. S. Department of Energy (DOE), Office of Science, Office of Basic Energy Sciences (BES), under Contract No. DE-AC02-06CH11357. S.K.S. acknowledges support from DOE BES Grant No. DE-FG02-04ER46173. We thank Tom Russell and Jinbo He at University of Massachusetts Amherst, Edward J. Kramer at University of California Santa Barbara, and Gila Stein at University of Houston for sharing the experiment GISAXS data used in sections III A and III B.

* zjiang@aps.anl.gov
† Present address: Department of Physics, Soongsil University, Seoul 156-743, Korea
‡ wangj@aps.anl.gov

[1] J. Wang, M. J. Bedzyk, T. L. Penner, and M. Caffrey, Nature **354**, 377 (1991).
[2] J. Wang, M. J. Bedzyk, and M. Caffrey, Science **258**, 775 (1992).
[3] Y. P. Feng, S. K. Sinha, H. W. Deckman, J. B. Hastings, and D. P. Siddons, Phys. Rev. Lett. **71**, 537 (1993).
[4] M. J. Bedzyk, G. M. Bommarito, and J. S. Schildkraut, Phys. Rev. Lett. **62**, 1376 (1989).
[5] S. Narayanan, D. R. Lee, R. S. Guico, S. K. Sinha, and J. Wang, Phys. Rev. Lett. **94**, 145504 (2005).
[6] D. R. Lee, A. Hagman, X. Li, S. Narayanan, J. Wang, and K. R. Shull, Appl. Phys. Lett. **88**, 153101 (2006).
[7] D. Babonneau, S. Camelio, D. Lantiat, L. Simonot, and A. Michel, Phys. Rev. B **80**, 155446 (2009).
[8] G. Renaud, R. Lazzari, and F. Leroy, Surf. Sci. Rep. **64**, 255 (2009).
[9] D.-M. Smilgies, P. Busch, C. M. Papadakis, and D. Posselt, Synchrotron Rad. News **15**, 35 (2002).
[10] B. Lee, J. Yoon, W. Oh, Y. Hwang, K. Heo, K. S. Jin, J. Kim, K.-W. Kim, and M. Ree, Macromolecules **38**, 3395 (2005).
[11] B. Lee, I. Park, J. Yoon, S. Park, J. Kim, K.-W. Kim, T. Chang, and M. Ree, Macromolecules **38**, 4311 (2005).
[12] P. Busch, M. Rauscher, D.-M. Smilgies, D. Posselt, and C. M. Papadakis, J. Appl. Cryst. **39**, 433 (2006).
[13] P. Busch, D. Posselt, D.-M. Smilgies, M. Rauscher, and C. M. Papadakis, Macromolecules **40**, 630 (2007).
[14] S. Jin, J. Yoon, K. Heo, H.-W. Park, J. Kim, K.-W. Kim, T. J. Shin, T. Chang, and M. Ree, J. Appl. Cryst. **40**, 950 (2007).
[15] G. E. Stein, E. J. Kramer, X. Li, and J. Wang, Macromolecules **40**, 2453 (2007).
[16] J. Yoon, S. Y. Yang, B. Lee, W. Joo, K. Heo, J. K. Kim, and M. Ree, J. Appl. Cryst. **40**, 305 (2007).
[17] J. Yoon, K. S. Jin, H. C. Kim, G. Kim, K. Heo, S. Jin, J. Kim, K.-W. Kim, and M. Ree, J. Appl. Cryst. **40**, 476 (2007).
[18] S. Park, D. H. Lee, J. Xu, B. Kim, S. W. Hong, U. Jeong, T. Xu, and T. P. Russell, Science **323**, 1030 (2009).
[19] Y. Lin, A. Böker, J. He, K. Sill, H. Xiang, C. Abetz, X. Li, J. Wang, T. Emrick, S. Long, Q. Wang, A. Balazs, and T. P. Russell, Nature **434**, 55 (2005).
[20] S. Narayanan, D. R. Lee, A. Hagman, X. Li, and J. Wang, Phys. Rev. Lett. **98**, 185506 (2007).
[21] S. Streit, C. Gutt, V. Chamard, A. Robert, M. Sprung, H. Sternemann, and M. Tolan, Phys. Rev. Lett. **98**, 047801 (2007).
[22] G. Renaud, R. Lazzari, C. Revenant, A. Barbier, M. Noblet, O. Ulrich, F. Leroy, J. Jupille, Y. Borensztein, C. R. Henry, J.-P. Deville, F. Scheurer, J. Mane-Mane, and O. Fruchart, Science **300**, 1416 (2003).
[23] C. Revenant, F. Leroy, R. Lazzari, G. Renaud, and C. R. Henry, Phys. Rev. B **69**, 035411 (2004).
[24] F. Leroy, G. Renaud, A. Letoublon, R. Lazzari, C. Mottet, and J. Goniakowski, Phys. Rev. Lett. **95**, 185501 (2005).
[25] M. Schmidbauer, D. Grigoriev, M. Hanke, P. Schäfer, T. Wiebach, and R. Köhler, Phys. Rev. B **71**, 115324 (2005).
[26] R. Lazzari, G. Renaud, J. Jupille, , and F. Leroy, Phys. Rev. B **76**, 125412 (2007).
[27] I. A. Vartanyants, A. V. Zozulya, K. Mundboth, O. M. Yefanov, M.-I. Richard, E. Wintersberger, J. Stangl, A. Diaz, C. Mocuta, T. H. Metzger, G. Bauer, T. Boeck, and M. Schmidbauer, Phys. Rev. B **77**, 115317 (2008).
[28] A. V. Zozulya, O. M. Yefanov, I. A. Vartanyants, K. Mundboth, C. Mocuta, T. H. Metzger, J. Stangl, G. Bauer, T. Boeck, and M. Schmidbauer, Phys. Rev. B **78**, 121304(R) (2008).
[29] M. P. Tate, V. N. Urade, J. D. Kowalski, T.-C. Wei, B. D. Hamilton, B. W. Eggiman, and H. W. Hillhouse, J. Phys. Chem. B **110**, 9882 (2006).
[30] M. Rauscher, R. Paniago, H. Metzger, Z. Kovats, J. Domke, J. Peisl, H.-D. Pfannes, J. Schulze, and I. Eisele, J. Appl. Phys. **86**, 6763 (1999).
[31] R. Lazzari, J. Appl. Cryst. **35**, 406 (2002).
[32] R. Lazzari, F. Leroy, and G. Renaud, Phys. Rev. B **76**, 125411 (2007).
[33] X. Hu, Z. Jiang, S. Narayanan, X. Jiao, A. R. Sandy, S. K. Sinha, L. B. Lurio, and J. Lal, Phys. Rev. E **74**, 010602(R) (2006).
[34] M. K. Mukhopadhyay, X. Jiao, L. B. Lurio, Z. Jiang, J. Stark, M. Sprung, S. Narayanan, A. R. Sandy, and S. K. Sinha, Phys. Rev. Lett. **101**, 115501 (2008).
[35] M. K. Mukhopadhyay, L. B. Lurio, Z. Jiang, X. Jiao, M. Sprung, C. DeCaro, and S. K. Sinha, Phys. Rev. E **82**, 011804 (2010).
[36] L. G. Parratt, Phys. Rev. **95**, 359 (1954).
[37] I. Kegel, T. H. Metzger, A. Lorke, J. Peisl, J. Stangl, G. Bauer, K. Nordlund, W. V. Schoenfeld, and P. M. Petroff, Phys. Rev. B **63**, 35318 (2001).
[38] S. K. Sinha, E. B. Sirota, S. Garoff, and H. B. Stanley, Phys. Rev. B **38**, 2297 (1988).
[39] V. Holý, J. Kuběna, I. Ohlídal, K. Lischka, and W. Plotz, Phys. Rev. B **47**, 15896 (1993).
[40] J.-P. Schlomka, M. Tolan, L. Schwalowsky, O. H. Seeck, J. Stettner, and W. Press, Phys. Rev. B **51**, 2311 (1995).
[41] M. Tolan, *X-Ray Scattering from Soft-Matter Thin Films* (Springer, Berlin, 1999).
[42] L. I. Schiff, *Quantum Mechanimcs* (McGraw-Hill, New York, 1968).
[43] J. S. Pedersen, J. Appl. Cryst. **27**, 595 (1994).
[44] R. Pynn, Phys. Rev. B **45**, 602 (1992).
[45] S. K. Sinha, M. Tolan, and A. Gibaud, Phys. Rev. B **57**, 2740 (1998).
[46] R. Hosemann and S. N. Bagchi, Acta Cryst. **5**, 612 (1952).
[47] B. K. Vainshtein, *Diffraction of X-Rays by Chain Molecules* (Elsevier, Amsterdam, 1966) Chap. V.

[48] G. Vignaud, A. Gibaud, J. Wang, S. K. Sinha, J. Daillant, G. Grübel, and Y. Gallot, J. Phys.: Condens. Matter **9**, L125 (1997).
[49] J. K. Percus and G. J. Yevick, Phys. Rev. **110**, 1 (1958).
[50] D. J. Kinning and E. L. Thomas, Macromolecules **17**, 1712 (1984).
[51] T. Sun, S. Donthu, M. Sprung, K. DAquila, Z. Jiang, A. Srivastava, J. Wang, and V. P. Dravid, Acta Mater. **57**, 1095 (2009).
[52] J. Y. Lee, Z. Shou, and A. C. Balazs, Phys. Rev. Lett. **91**, 136103 (2003).
[53] J. He, R. Tangirala, T. Emrick, T. P. Russell, A. Böker, X. Li, and J. Wang, Adv. Mater. **19**, 381 (2007).
[54] R. Hosemann and S. N. Bagchi, *Direct Analsysis of Diffraction by Matter* (North-Holland, Amsterdam, 1962).
[55] Q. Li, J. He, E. Glogowski, X. Li, J. Wang, T. Emrick, and T. P. Russell, Adv. Mater. **20**, 1462 (2008).
[56] G. E. Stein, W. B. Lee, G. H. Fredrickson, E. J. Kramer, X. Li, and J. Wang, Macromolecules **40**, 5791 (2007).
[57] M. Schmidbauer, *X-Ray Diffuse Scattering from Self-Organized Mesoscopic Semiconductor Structures* (Springer, Berlin, 2004).